JOURNAL OF GUIDANCE, CONTROL, AND DYNAMICS
Vol. 34, No. 4, July–August 2011

Control Evaluations of Semiactive Fluid–Elastomeric Helicopter Lag Damper

Curt S. Kothera*
Techno-Sciences, Inc., Beltsville, Maryland 20705
and
Grum T. Ngatu† and Norman M. Wereley‡
University of Maryland, College Park, Maryland 20742

DOI: 10.2514/1.51434

A semiactive magnetorheological fluid–elastomeric device has been assembled and evaluated in control experiments to demonstrate its utility to compensate for measured changes as a helicopter lag damper. The baseline used in this study was lag damper (snubber) for a hingeless helicopter rotor that employs both elastomers and fluids: that is, a fluid–elastomeric damper. This damper was disassembled and modified to include two internal magnetorheological control valves, and the existing hydraulic fluid was replaced with magnetorheological fluid. Hence, the resulting prototype damper is a retrofit design that can easily be installed in a test rotor in future evaluations. The magnetorheological fluid–elastomeric damper was subject to extensive performance characterization at displacement amplitudes ranging from 0.8 to 3.4 mm, temperatures ranging from 20 to 55°C, and control currents up to 2.0 A. Using this database and a hydromechanical model of the damper, control systems were designed to track a reference damping profile, which is a function of amplitude only, in the presence of measured amplitude and temperature variations at the rotor lag frequency (3.8 Hz). Both open-loop (interpolating lookup table) and closed-loop (proportional-integral and gain scheduling) techniques were employed in simulations and experiments. The results demonstrated that all of the control schemes were effective, although a minimum tracking error was achieved with the closed-loop systems. Comparing the two closed-loop systems, the gain-scheduling controller provided a faster response overall, but the improvement was marginal.

Nomenclature

b_m = finite impulse response filter coefficient
C_A = passive viscous damping, Ns/mm
C_{eq} = equivalent damping, Ns/mm
C_5 = chamber compliance damping, Ns/mm
C_{r5} = shear damping of elastomer, Ns/mm
C_{eq}^* = target damping, Ns/mm
d = gap thickness, mm
D_o = flux return outer diameter, mm
e = energy dissipation error, J
E_{dis} = energy dissipated, J
f = force, N
F_c = first force Fourier cosine component, N
F_s = first force Fourier sine component, N
F_y = yield force of magnetorheological fluid, N
f_{lag} = rotor lag frequency, Hz
i = current, A
J = cumulative error metric, J^2 s
k_I = integral gain, A/Js
k_P = proportional gain, A/J
k_{r5} = shear stiffness of elastomer, N/mm
k_5 = chamber bulge stiffness, N/mm
k^* = complex stiffness, N/mm
k' = in-phase stiffness, N/mm
k'' = quadrature stiffness, N/mm
L_c = active valve length, mm
L_p = total valve length, mm
m_A = effective mass of magnetorheological fluid, kg
m_{r5} = effective mass of elastomer, kg
N = number of samples per period
r = bobbin radius, mm
T = temperature, °C
t = time, s
T_f = final time, s
T_p = period, s
t_R = response time metric, s
w = finite impulse response filter input
X = displacement amplitude, mm
x = displacement, mm
X_c = first displacement Fourier cosine component, mm
X_s = first displacement Fourier sine component, mm
x_A = effective displacement of fluid in magnetorheological valve, mm
η = loss factor
ψ = valve factor
ω_{lag} = rotor lag frequency, rad/s

Introduction

AEROMECHANICAL stability of helicopters is a nonlinear phenomenon involving complex interactions of aerodynamic, inertial, and elastic forces. Because of stress and weight considerations, advanced rotors are typically soft in-plane, which makes them more susceptible to aeromechanical instabilities, such as air and ground resonance [1,2]. However, with the emergence of these soft-in-plane (hingeless or bearingless) rotors, conventional hydraulic piston lead–lag dampers exhibit a large reduction in damping as the amplitude of motion increases, leading to excessive size and weight in the dampers in order to accommodate all operating conditions. As a result, elastomeric lead–lag dampers were introduced in an effort to improve upon the performance capabilities of hydraulic devices

---

Received 2 July 2010; revision received 22 February 2011; accepted for publication 26 February 2011. Copyright © 2011 by C. S. Kothera, G. Ngatu, and N. M. Wereley. Published by the American Institute of Aeronautics and Astronautics, Inc., with permission. Copies of this paper may be made for personal or internal use, on condition that the copier pay the $10.00 per-copy fee to the Copyright Clearance Center, Inc., 222 Rosewood Drive, Danvers, MA 01923; include the code 0731-5090/11 and $10.00 in correspondence with the CCC.

[*] Research Engineer; kotherac@technosci.com. Senior Member AIAA.

[†] Graduate Research Assistant and Sloan Fellow, Smart Structures Laboratory, Department of Aerospace Engineering; grum@umd.edu. Student Member AIAA.

[‡] Professor and Associate Chair, Smart Structures Laboratory, Department of Aerospace Engineering; wereley@umd.edu. Associate Fellow AIAA.

[3–7]. However, elastomeric lead–lag dampers tend to present damping loss for very small amplitudes, as well as large variations in stiffness and damping as temperature varies [8]. Despite continued improvement in material performance, some articulated rotors require more damping than current elastomers can achieve, and this is particularly true for rotors that were originally designed to use hydraulic lead–lag dampers. The greatest amount of lag mode damping at the lowest cost (both initial and maintenance) is desirable.

Advanced rotor systems have begun to adopt fluid-elastomeric (FE) damping solutions in an effort to combine the strengths of both (hydraulic) fluid dampers and elastomeric dampers [9]. However, these advanced lead–lag dampers are passive devices and can still only operate with a single damping profile. Additionally, the elastomeric materials used in these devices exhibit temperature-dependent behavior that causes stiffness and damping properties to deviate [10,11], as does the hydraulic fluid viscosity change with temperature.

Semiactive lead–lag dampers employing field-controllable fluids, such as magnetorheological (MR) fluids, have demonstrated the potential to greatly improve damper performance by providing a means by which to augment damping in real time [12–14]. By employing MR technology with advanced FE devices to create a magnetorheological fluid-elastomeric (MRFE) lag damper, the ability to augment or optimize damping in flight is born [15]. This preliminary examination into the potential benefits of combining the features of MR fluids with elastomeric materials showed that the damping contributions of each were additive and that amplitude-dependent losses in performance from the elastomer component could be restored by the adjustable MR component. Adjusting stability margins in flight for optimal characteristics could potentially increase forward speed, maneuverability, and payload capacity in a broadened operational environment.

Control studies have taken place to explore the potential that semiactive dampers have for advanced rotor systems. Feedback linearization techniques, in particular, have shown success. For example, when a four-bladed rotor suffers damage and loses up to 50% damping capacity in one or two of the blades, MR dampers were shown to have the ability to stabilize this unstable rotor system, although stability could not be recovered from 100% loss of damping in one blade [2]. Ground resonance stabilization and reduced periodic damper loads were shown to be achievable using MR dampers as well [16]. Additionally, limit-cycle instability can be eliminated with high damping ratios, and the resulting high periodic loads during forward flight can be eliminated by introducing a band-rejecting filter to the feedback signal [17]. However, these investigations have all considered linear stroke MR dampers.

With the trend of hingeless rotors beginning to overtake articulated rotors, these past studies on conventional linear stroke piston-type dampers become less applicable to the newer snubber-type dampers that have no moving parts and dissipate energy primarily by volumetric changes in their soft body that force fluid to flow through static ports. Hence, the need exists to investigate the adaptability of these dampers intended for soft-in-plane rotors. The focus of this work is to explore the control capabilities of a prototype MRFE damper in terms of tracking a target damping profile in the presence of changing displacement amplitude, as well as variations in ambient temperature, which are more pronounced in a damper for which the body is mostly elastomeric. Development of the retrofit prototype damper will be discussed, followed by controller design. Three control techniques will be designed, implemented, experimentally evaluated, and compared for steady-state error and response time over the amplitude and temperature ranges tested. The paper will close with conclusions and a plan for future work.

Magnetorheological Fluid–Elastomeric Damper Development

The laboratory prototype was a snubber lag damper modified to incorporate two control valves and MR fluid as a retrofit unit. The existing lag damper is pictured in Fig. 1a, and it served as the baseline for comparison throughout this investigation. Figure 1b shows the assembled MRFE retrofit damper with internal MR valves (not visible). The two plugs on either side of the center bolt (top) provide a means of supplying the control current to the two internal MR valves.

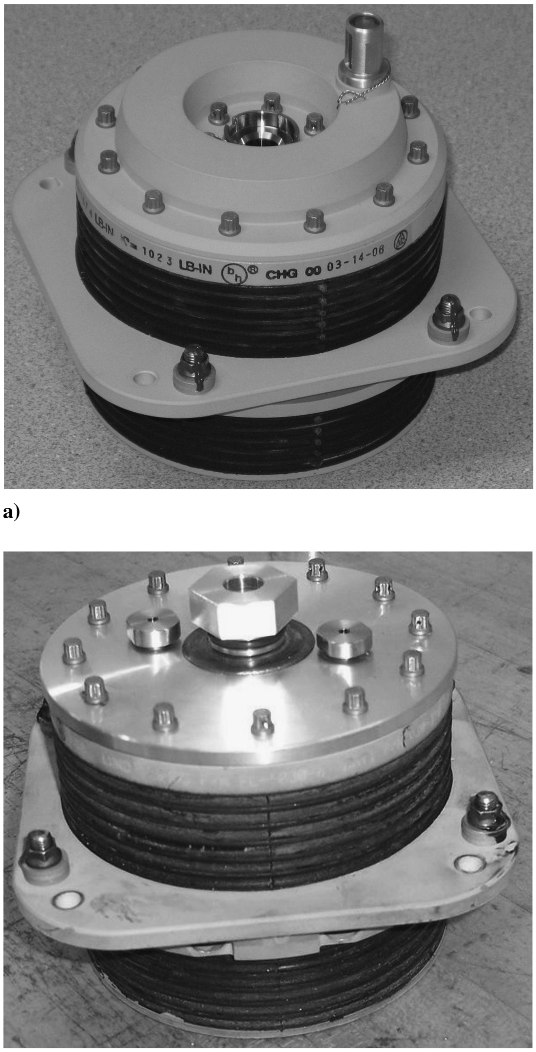
a)

b)

Fig. 1 Hingeless rotor lag dampers: a) baseline damper and b) modified MRFE damper.

Figure 2 shows a partial section view of the prototype damper without the MR control valves installed. The cylindrical body of the FE damper is made of a multiple lamination of metallic and elastomeric ring layers, with a metal plate midway along the body axis. The

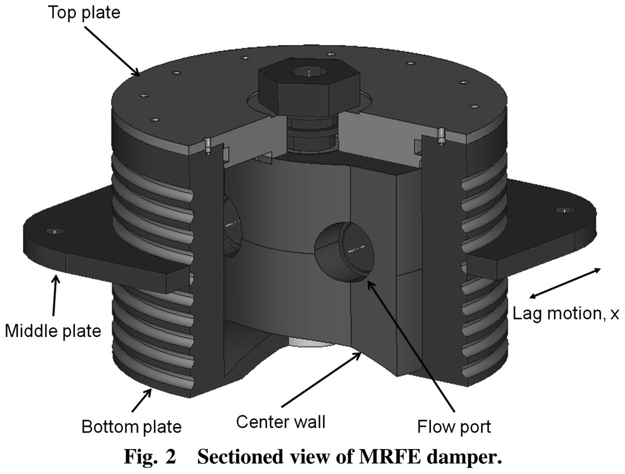

Fig. 2 Sectioned view of MRFE damper.

primary (viscous) damping component of the device is enabled through a vertical, elastomeric center wall that contains two flow ports. This wall essentially separates the internal damper cavity into two fluid reservoirs. Note that the baseline damper is assembled as a molded unit, so there is no possibility for fluid to be exchanged from one reservoir to the other without passing through one of the flow ports. It is the relative motion between this middle plate and the top and bottom plates (moving together) that constitutes damping motion. As the middle plate moves relative to the top and bottom plates in a shearing motion, the deformation of the elastomeric body and center wall creates a pressure differential between the two fluid chambers, and viscous flow is induced.

In an effort to minimally modify the baseline damper, the two MR valves were installed into the two existing flow ports (one valve in each fluid chamber). A detailed schematic of the MR valve is provided in Fig. 3. The valve is composed of a bobbin, upon which the electromagnetic coil is wound, and a flux return. As it appears in the figure on the left, the flux return of the MR valve has the general shape of a stepped cylinder, with the larger diameter portion housing the bobbin and coil, and the smaller diameter portion threaded to fit inside the damper flow port. Fluid flows from one chamber through the annular gap in the valve, where it can be activated, to the other chamber. The key design variables associated with the MR valve are labeled in Fig. 3 on the right. The annular gap thickness d can be varied by changing the radius of the bobbin r or changing the inner diameter of the flux return ring, and the active valve length L_c can be adjusted to increase or decrease the magnetic flux that activates the MR fluid. Specified by the flux return outer diameter D_o and the valve length L_p the maximum size of the valve must be such that it does not impede the motion of the damper. Note also that the magnetic field lines are illustrated by arrows. More details of the MR valve design can be found in [18].

With the valves installed in the prototype MRFE damper, a set of performance characterization experiments was conducted to evaluate the range of achievable damping augmentation. A fixture was designed to hold the damper in a servohydraulic testing machine and to allow the test machine to simulate the lead–lag motion experienced on the rotor, albeit in the fixed frame (Fig. 4). Note that this passive damper was also tested to provide a basis of comparison for the MRFE damper. The load cell at the top measured the damper force output, and the actuator on the bottom generated the displacement input to the damper. In the case of the MRFE damper, there was also a dc power supply to apply current to the control valves.

For all of the experimental evaluations to be discussed, the actuation frequency used is the rotor lag frequency of 3.8 Hz. The displacement amplitudes used on the sinusoidal excitations varied from 30 mils (0.762 mm) to 130 mils (3.81 mm) in increments of 20 mils (0.50 mm), while the applied current was varied from 0.0 to 2.0 A in increments of 0.25 below 1.0 A and increments of 0.50 above 1.0 A. Different increments in current were used here, because the adjustable damping sensitivity decreases as the current level increases, up to the point of saturation, which occurs shortly above 2.0 A. For computation of the damping metric (equivalent damping), the complex modulus method was employed. This linear technique assumes that the complex damper stiffness k^* is a combination of the in-phase stiffness k' and the loss stiffness k'':

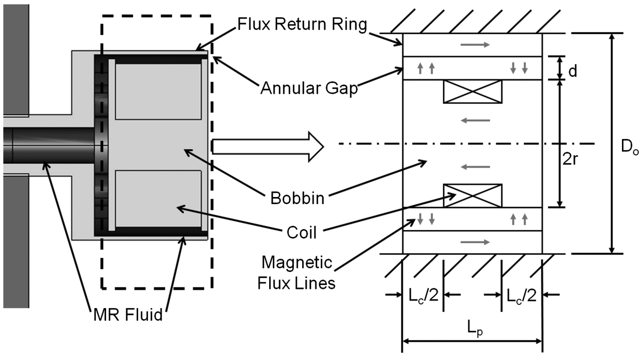

Fig. 3 Details of MR control valve.

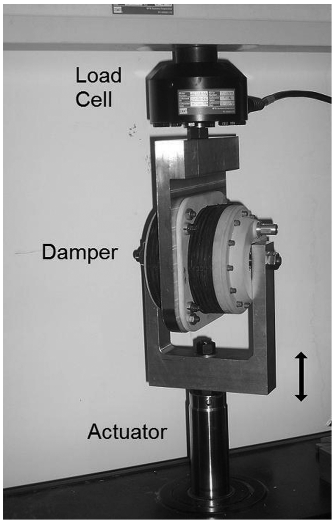

Fig. 4 Test setup for experimental characterization.

$$k^* = k' + jk'' = k'(1 + j\eta)$$

where η is the loss factor or the ratio of loss stiffness to in-phase stiffness. The damper force is estimated by the first Fourier sine and cosine components, F_s and F_c, respectively, at the fundamental frequency ω_{lag} ($f_{\text{lag}} = 3.8$ Hz) as

$$f(t) = F_s \sin(\omega_{\text{lag}} t) + F_c \cos(\omega_{\text{lag}} t) = k' x(t) + \frac{k''}{\omega_{\text{lag}}} \dot{x}(t)$$

The stiffnesses k' and k'' are determined by substituting the displacement function $[x(t) = X_s \sin(\omega t) + X_c \cos(\omega t)]$ and its derivative into the preceding equation:

$$k' = \frac{F_c X_c + F_s X_s}{X_c^2 + X_s^2} \qquad k'' = \frac{F_c X_s - F_s X_c}{X_c^2 + X_s^2}$$

The equivalent damping C_{eq} is then approximated from the loss stiffness by

$$C_{\text{eq}} \cong \frac{k''}{\omega_{\text{lag}}}$$

Note that this is an approximation, because the complex stiffness assumes steady-state harmonics at the excitation frequency (ω_{lag}), but it remains perfectly reasonable to compare the performance of two dampers.

The performance comparison between the baseline damper and the prototype MRFE damper is presented in Fig. 5. As shown, equivalent damping (Fig. 5a) and stiffness (Fig. 5b) of the baseline passive damper (dashed lines) is a single profile that has some linear dependence on displacement amplitude. However, the MRFE damper demonstrates a controllable range through application of the constant current levels indicated in the legends. This is most pronounced in the damping. At 0 A, the same trend seen with the baseline damper is apparent in the MRFE damper, but it is shifted downward. This decrease in field-off damping is, by design, to enable the potential to reduce damping forces on rotor components. Applying increased amounts of current then cause the damping to increase incrementally until saturation (near 2 A), although the slope with respect to amplitude does shift from positive to negative at higher currents. This leaves the entire range between 0 A and saturation as achievable damping levels at each amplitude, from which damping optimization can take place. Similar trends are also apparent with the in-phase stiffness, although the low amplitude stiffness is proportionally high compared with that at higher amplitudes. This is attributable to the reduced velocity and pressure that limit flow through the activated MR valves. Note that the

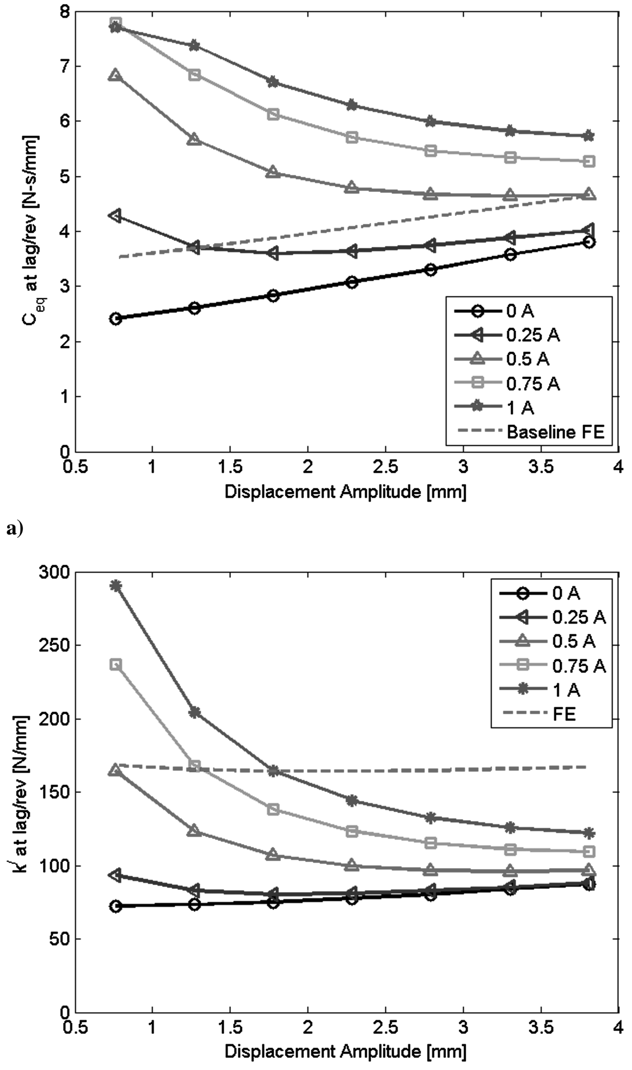

a)

b)

Fig. 5 Damper performance characterization at lag frequency: a) equivalent damping; (b) stiffness.

baseline performance and controllable property ranges can both change substantially from these characteristics as the temperature varies from the ambient [19].

The apparent reduction in stiffness (Fig. 5b) of the MRFE damper when compared with the baseline should also be discussed briefly, since increasing current does not produce the same enveloping effect that was seen in the damping results (Fig. 5a). Recall that the prototype MRFE damper was a retrofit design of the baseline damper, and that the baseline damper was assembled as a molded unit. To convert the baseline damper into the MRFE damper, part of its molded interior had to be destructively disassembled to gain access to the fluid chambers and install the MR valves. This destructive disassembly led to a reduction in stiffness when the damper was reassembled, because the material could not be remolded together. Note that the stiffness of the damper is primarily due to the elastomeric body, which was affected during disassembly, but the damping is primarily due to the fluid passing through the flow ports, which was not affected during disassembly. Hence, the damping envelopes the baseline damper performance, as designed, but the stiffness does not envelope the baseline performance, although it still shows variation with applied current, which is the general function of the retrofit device. Building this MRFE damper with MR control installed from the outset would eliminate the shown stiffness reduction and provide a similar enveloping effect around the baseline performance to that which is visible for the damping profiles.

Magnetorheological Fluid–Elastomeric Damper Model Summary

Recent effort was also placed on establishing a predictive design tool that can be used in future design revision of the present retrofit device, in addition to translating the key phenomena to completely different MRFE damper configurations [20]. Thus, a lumped parameter, hydromechanical model was derived using MR valve dimensions, internal geometry of the fluid chambers, and properties of the electromagnetic coil, MR fluid, and damper elastomer as the underlying basis. Effects of parameter variation due to temperature have also recently been included in both the model of the existing baseline fluid–elastomeric damper [11] and the prototype MRFE damper [19]. The resulting model was used to aid in the design of the control systems and will be briefly introduced here.

The analogous mechanical system is shown in Fig. 6. Here, m_A is the inertial effect of the MR fluid and C_A is the passive viscous damping effect due to flow resistance in the MR valves and port holes. The shear stiffness and damping of the elastomeric portion of the damper body are represented by k_{r5} and C_{r5}, respectively. The fluid chamber bulge stiffness and compliance damping are given by k_5 and C_5. Controllable damping enters into the system through F_{yA}, which represents the field-controllable yield force of the MR fluid passing through the valves. Note that the initial model derivation was for the general case where the valves and flow ports were not necessarily the same, but these are identical for the prototype MRFE damper, causing the equivalences and reduced form shown (e.g., $k_{r1} = k_{r5}$, $k_1 = k_5$, $C_1 = C_5$, $C_{r1} = C_{r5}$, and $\psi = 1$). Given an input displacement to the damper of $x(t)$, the force response can be computed according to

$$
\begin{aligned}
&2m_{r5}\ddot{x}(t) + 2C_{r5}\dot{x}(t) + 2k_{r5}x(t) + 2C_5[\dot{x}(t) - 2\dot{x}_A(t)] \\
&\quad + 2k_5[x(t) - 2x_A(t)] = f(t) \\
&m_A\ddot{x}_A(t) + C_A\dot{x}_A(t) - 2C_5[\dot{x}(t) - 2\dot{x}_A(t)] - 2k_5[x(t) - 2x_A(t)] \\
&\quad + F_{yA}\mathrm{sgn}[\dot{x}_A(t)] = 0
\end{aligned}
$$

where x_A is the generalized internal model displacement. For the MRFE damper, the preyield behavior is a function of m_A, C_5, and k_5, implying that the preyield stiffness is dominated by the fluid chamber compliances, while the postyield behavior is governed primarily by C_A and F_{yA}. This set of equations does appear to be fairly simple, but it must be noted that the key parameters involved have the following dependencies on displacement amplitude X, temperature T, and applied current i:

$$
\begin{gathered}
C_{r5} = C_{r5}(X, T) \qquad k_{r5} = k_{r5}(X, T) \qquad C_5 = C_5(X, T) \\
k_5 = k_5(X, T) \qquad C_A = C_A(T) \qquad F_{yA} = F_{yA}(i)
\end{gathered}
$$

These parameter dependencies imply that the MRFE lag damper has three inputs, two of which cannot be directly controlled (displacement and temperature). However, it is the other (current) that can be

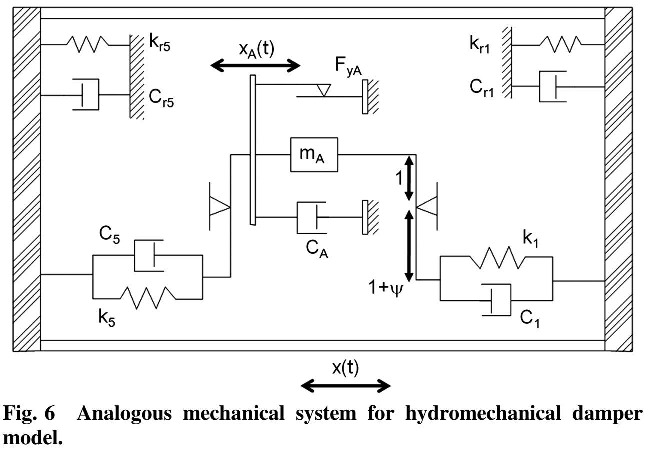

Fig. 6 Analogous mechanical system for hydromechanical damper model.

adjusted to compensate for force level variations due to these two inputs, giving the possibility of multiple operating points. Hence, this prospect of obtaining optimal damping profiles motivates the exploration of control techniques with the MRFE damper.

Control Design

The utility of three different control schemes was evaluated in terms of tracking a reference damping profile that was a function of only displacement amplitude, although temperature was also varied from 30 to 55°C. In this fixed frame, feasibility study, the unmodified damper performance at room temperature (∼30°C) and rotor lag frequency (3.8 Hz) was selected as the target profile over an amplitude range of 0.8 to 3.4 mm. Recall that this is the dashed line in Fig. 5. In each of the three control techniques employed, two real-time measurements are required, although they are not necessarily the same for each technique.

Computation of Performance Metric

The performance metric discussed previously was the equivalent damping. This works well for characterizing damper performance and in designing an open-loop controller, but it does require extra computations and more knowledge of the signals, which could increase complexity of a control system to be integrated with a helicopter. Equivalent damping C_{eq} can alternatively be computed as

$$C_{\mathrm{eq}} = \frac{E_{\mathrm{dis}}}{\pi \omega_{\mathrm{lag}} X^2}$$

where E_{dis} is the energy dissipated, ω_{lag} is the rotor lag frequency, and X is the stroke amplitude. From this equation, it can be seen that C_{eq} is proportional to E_{dis}, but it also requires frequency and amplitude information. Hence, using the energy dissipated as the performance metric would certainly reduce the number of computations that must be performed, especially since the stroke amplitude must be computed (estimated) from a displacement sensor signal. It is calculated as

$$E_{\mathrm{dis}} = \int_0^{T_p} f(x)\,\mathrm{d}x$$

where $f(x)$ is the damper output force in response to the input stroke $x(t)$, and the integration occurs over one period T_p. For the rotor lag frequency of 3.8 Hz for the current prototype damper, this is 0.26 s.

Based on the target damping profile at the rotor lag frequency, the target energy dissipation profile can be calculated directly from the preceding C_{eq} equation. Figure 7 shows the target damping profile in the upper plot (from Fig. 5) and its associated target energy dissipation profile in the lower plot. There is very little (near zero) energy dissipation at the lowest amplitude, and this increases nonlinearly to 4 J at the high end of the displacement amplitude range. It should be noted here that the target profile used in this study is that of the existing system, which was constrained by the passive fluid–elastomeric technology. The ability to vary damping capacity in real time would undoubtedly change the target profile, but it would require a completely new rotor dynamic design analysis, which was outside the scope of the current effort. Demonstrating that the MRFE damper performance could match the existing profile across a range of temperatures was deemed to be a sufficient demonstration of the semiactive technology and helps motivate a more thorough study design.

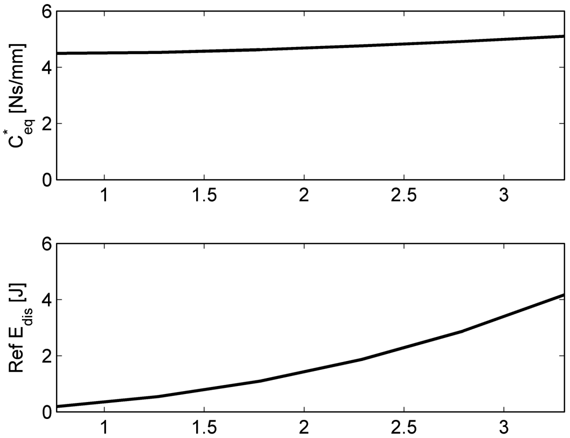

Fig. 7 Desired damping and energy dissipation levels.

A secondary advantage of using energy dissipation as the performance metric of choice for the MRFE lag damper, although still following along the justification for reduced computations, is that it will be directly applicable to a closed-loop control system that uses damping (energy dissipated) as a feedback variable. Details of this approach are presented next, and the possibility exists for the helicopter pilot to have the ability to adjust the energy dissipation (damping) by simply turning a knob in the cockpit.

It was shown previously that two measurement signals are integrated (force with respect to displacement) over one period to calculate energy dissipation. To implement this in a digital control system, a series of discrete transfer functions can be assembled to perform the base operations. Two discrete transfer functions that perform a difference operation of the form

$$B(z) = \frac{z-1}{z}$$

and a unit delay

$$A(z) = \frac{1}{z}$$

all having zero initial conditions, can be used to calculate the elements of a trapezoidal integral estimate over one time step. The change in displacement follows as

$$\Delta x_n = x[n] - x[n-1]$$

where n is the current time step, and the change in force is

$$f_n = \tfrac{1}{2}(F[n] - F[n-1]) + F[n-1]$$

Having these two elements, integration over one period can be performed:

$$E_{\mathrm{dis}} = \sum_{n=1}^{N} f_n \Delta x_n$$

which essentially adds a preselected number of values together. Since the sample rate of the controller would be known before implementation, the number of data samples that occur over one period can easily be calculated. It has been assumed here that the period of interest is the rotor lag period, although this could be changed without consequence to the method. Knowing the number of samples per period N, a finite impulse response (FIR) filter can be designed to estimate the energy dissipated over the period of interest. The general form is [21]

$$y[n] = \sum_{m=0}^{N} b_m w[n-m]$$

where $y[n]$ is the output (in this case, E_{dis}), $w[n-m]$ are the inputs (in this case, $f_m \Delta x_m$), and b_m are the coefficients. Using a FIR filter simply for addition (integration) of previous points, the coefficients are specified by $b_m = 1$, for $m = 0, 1, \ldots, N$. This filter remembers only the previous N samples and adds them together with equal weighting for each. With each new time step, the filter will essentially forget the oldest sample and replace it with the new input value before performing the windowed summation. Note that this does, however, have an initial one-cycle delay until there are N measurement samples available. Substituting the δ function for the input of the filter gives the impulse response function form

$$h[n] = \sum_{m=0}^{N} b_m \delta[n-m] = b_n$$

From here, the z transform can be taken to arrive in the discrete domain form of the filter

$$H(z) = Z\{h[n]\} = \sum_{n=-\infty}^{n=\infty} h[n] z^{-n} = \sum_{n=0}^{N} b_n z^{-n}$$

Open-Loop Design

The open-loop control system has two inputs to a controller with one output, as shown in Fig. 8. A lookup table database was assembled based on MRFE damper characterization data at a number of control currents and temperatures. For each of the four temperatures (20, 30, 40, and 50°C), damper characterization data similar to those displayed in Fig. 5a were collected. With two inputs (estimation of displacement amplitude and measured internal temperature) and using the hydromechanical damper model, the open-loop controller was designed to select the appropriate control current i_{OLC} to match the target damping profile C^*_{eq} by two-dimensional interpolation or extrapolation:

$$i_{\mathrm{OLC}}(X, T) = \min_{i}\{C_{\mathrm{eq}}(X, T, i) - C^*_{\mathrm{eq}}(X)\}$$

Note that the displacement amplitude was calculated with a discrete FIR filter similar to that described previously for calculation of the dissipated energy, except that the filter coefficients were redefined for a moving average rather than the former windowed sum as

$$b_m = \frac{1}{N+1}$$

and the input to the filter was

$$w[n] = (x[n])^2$$

which, along with a square-root operation (yielding an rms value) and multiplication by $2^{1/2}$, gives the amplitude estimation of the past N samples. A rms estimation could have been employed similarly with no consequence, but since the database was already organized in terms of amplitudes, this approach was adopted here. It should also be noted here that this method of amplitude estimation, or calculation, differs from the more common Fourier transform, but it may be more appropriate for the present application because it requires only a single period of data (N samples) and is updated continuously to account for amplitude changes resulting from flight maneuvers, speed changes, gust loads, etc.

Parameterization of the open-loop controller with the experimental database gives the corresponding control currents that are displayed in Fig. 9. Here, in Fig. 9a, the entire range of the database is shown for the temperatures and displacement amplitudes used in the experimental damper characterization, while Fig. 9b shows a few discrete segments taken from the control currents to more clearly illustrate the general trends. It is seen here that the control current increases with amplitude and temperature in order to maintain the target damping profile. Note that the damping properties of the prototype device decrease with increasing temperature, primarily due to reduction in viscosity, which justifies the need to increase control current at higher temperatures in an effort to increase the yield force in the MR fluid. Looking over the entire range of inputs, the minimum current level (0.14 A) occurs at the smallest displacement amplitude (0.76 mm or 30 mils) and lowest temperature (20°C). Conversely, the maximum current level (0.86 A) occurs at the largest displacement amplitude (3.3 mm or 130 mils) and the highest temperature (50°C). Since the minimum current required was nonzero, this does imply that the presently designed prototype MRFE lag damper could match the target damping profile, defined as the 30°C performance of the baseline damper, at temperatures colder than 20°C. In the ideal case for the valve design approach taken here (low offstate damping), the damper performance with no current (0 A) would match the target damping profile at the coldest temperature of interest.

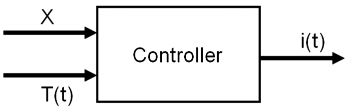

Fig. 8 Open-loop control approach.

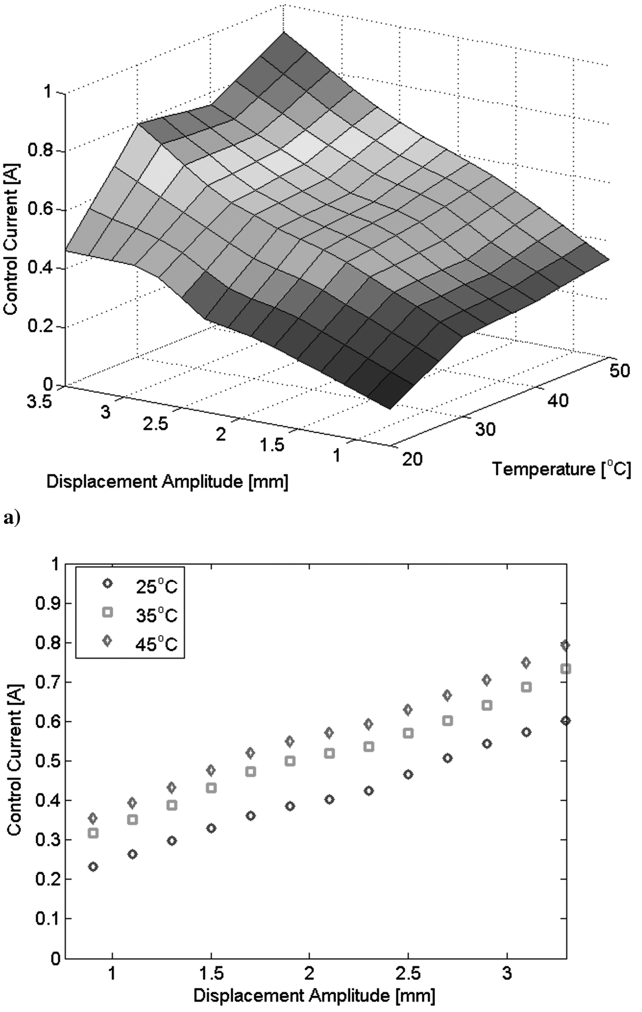

a)

b)

Fig. 9 Open-loop controller parameterization: a) range of database and b) distinct temperature profiles.

With this form of the controller parameterized from the experimental database, the open-loop control system (damper model included) was simulated at a few offdesign points to show that the interpolation functions were performing properly. These simulations were performed with constant stroke amplitude and constant temperature for the duration of each simulation and at the rotor lag frequency of 3.8 Hz. Figure 10 displays the results at 25°C (circles), 35°C (squares), and 45°C (diamonds) over the range of stroke amplitudes tested. The energy dissipation of the controlled MRFE lag damper model is shown in relation to the target profile (black dashed line). As can be seen, the open-loop controller has the ability to maintain the desired damping level, regardless of changes in stroke amplitude or temperature. There are two locations at the 25°C condition where deviation from the target profile is noticeable (near 1 mm and near 2.8 mm), but these deviations are all less than 10% error. Hence, the open-loop controller form has been validated.

Closed-Loop Design

While the open-loop controller was shown to accurately track a reference damping profile, one disadvantage of the technique is that

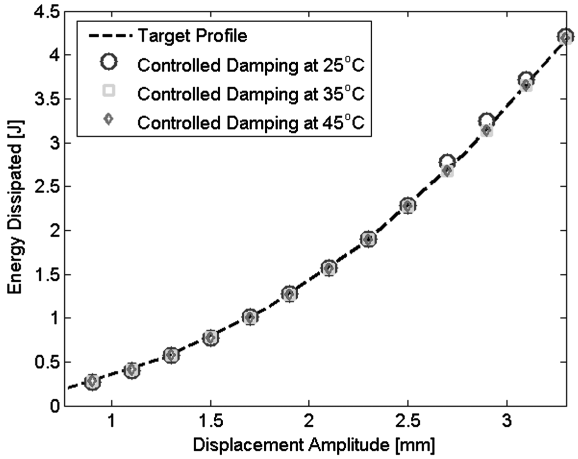

Fig. 10 Open-loop control simulation results at rotor lag frequency.

there is no measurement of accuracy or self-adjustment. With this in mind, closed-loop control was considered. The general diagram of the negative feedback system employed on the prototype MRFE damper is shown in Fig. 11, where the reference energy dissipation is denoted as Ref E_{dis} (function of displacement amplitude only in this study), e is the error signal or the difference between the desired energy dissipation and the actual (measured) energy dissipation (input to controller), i is the control current (output of controller), T and x are the respective temperature and displacement (inputs to damper), and f is the force (output of damper).

The control problem of interest in this investigation is reference tracking, as seen. As such, a proportional-integral (PI) control approach was selected. The hydromechanical damper model was modified to incorporate a PI controller, and a series of simulations was performed to optimize the control gains. Parameters varied in the optimization routine were displacement amplitude (seven total, ranging from 0.8 to 3.4 mm) and temperature (three total, ranging from 30 to 50°C). The proportional control gain was adjusted between 0 and 15, and the integral control gain was adjusted between 0 and 20 at each of the (amplitude, temperature) combinations. Two performance measures were considered in determining the best set of gains for each condition. The first was an error metric, which was computed at the end of each simulation according to

$$J = \int_0^{T_f} e^2(t)\,\mathrm{d}t$$

where J is a cumulative error metric and T_f is the final time of the simulation (3 s). Therefore, the control gains that produce the minimum value of J will be the ideal parameter for each case with respect to overall error. The error metric J gives an estimate for the optimal control gains based on overall error, but the time in which the closed-loop system can respond and begin to follow the desired energy dissipation level is also important. Accordingly, a response time metric t_R was considered in the design as the second performance measure. This value represents the time it takes for the closed-loop response (energy dissipated) to come within 10% of the desired level, based on the squared error computation. Figure 12 shows the effect that the control gains have on these closed-loop performance metrics at the smallest and largest displacement amplitudes, and at the maximum temperature, where the most deviation from the desired energy dissipation levels is present. One common trend in these results is that varying the proportional gain has little effect on the performance metric. The converse is seen for varying the integral gain, where the response spans a broad range of J and t_R. Additionally, there are clear minima with respect to k_I, and the minimum of J and t_R appear to occur at nearly the same value of k_I for a given displacement amplitude. At the maximum temperature condition shown, however, the minimum at 0.8 and at 3.4 mm do not coincide, indicating that amplitude dependence of the control gains may be required for the closed-loop system.

Similar to the previous figure, Fig. 13 has been included to show the simulation results at the lowest and highest displacement amplitudes while varying the integral gain and temperature, with the proportional gain fixed ($k_P = 0$). As seen in these figures, the temperature appears to have little effect on the optimal control gain at either of the amplitudes shown, much the same as was the case for the proportional gain in Fig. 12. For example, at $X = 0.8$ mm, the minimum J occurs from $8.6 < k_I < 9.8$, and at $X = 3.4$ mm, it occurs from $1.0 < k_I < 1.2$ over the temperature range simulated. There is a large variation in the optimal gain (minimum J) over the displacement amplitude range, however, varying nearly an order of magnitude from Figs. 13a–13c. Similar trends are also seen with the response time metric, again with the smallest amplitude in Fig. 13b and the largest amplitude in Fig. 13d. Note that the plateau regions seen at 3 s imply that the closed-loop system did not settle with those corresponding gains during the simulation. Also, as with the cumulative error, the response time metric is minimally dependent on temperature, with the minimum occurring from $7.8 < k_I < 8.6$ at 0.8 mm and $0.8 < k_I < 1.0$ at 3.4 mm, but it does show a large dependence on displacement amplitude. Conveniently, the best integral control gain from these two metrics nearly coincides at each of the amplitude and temperature settings. Figure 14 illustrates this at 50°C and 3.4 mm.

To more closely examine the amplitude dependency of the integral control gain, the optimal values from each of the two metrics are shown overlaying each other in Fig. 15 for the 30°C condition. Each point in this figure represents the minimum value of the associated metric, as shown in the previous set of figures. It is clear here that the optimal integral gains follow the same trend of high gain at small amplitude and low gain at large amplitude, and the gain values are nearly equivalent at each amplitude. Based on this similarity, an average value of k_I could be used between J and t_R. This does not consider the large variation with amplitude, however, which could potentially cause a decrease in performance for a controller with fixed gains. Hence, at this point, the decision was made to consider two closed-loop approaches. The first was a simpler PI controller with a single pair of gains (k_P and k_I), those being the average values chosen over the amplitude range of interest, and the second was a gain-scheduling PI controller, where the value of the gains would change using the real-time amplitude estimate as the scheduling variable

$$k_I = k_I(X)$$

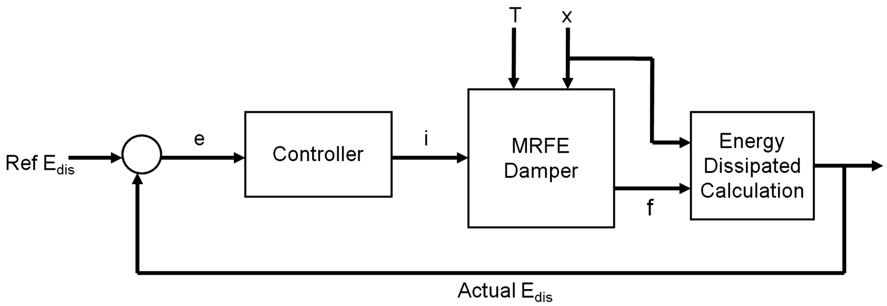

Fig. 11 Closed-loop control approach.

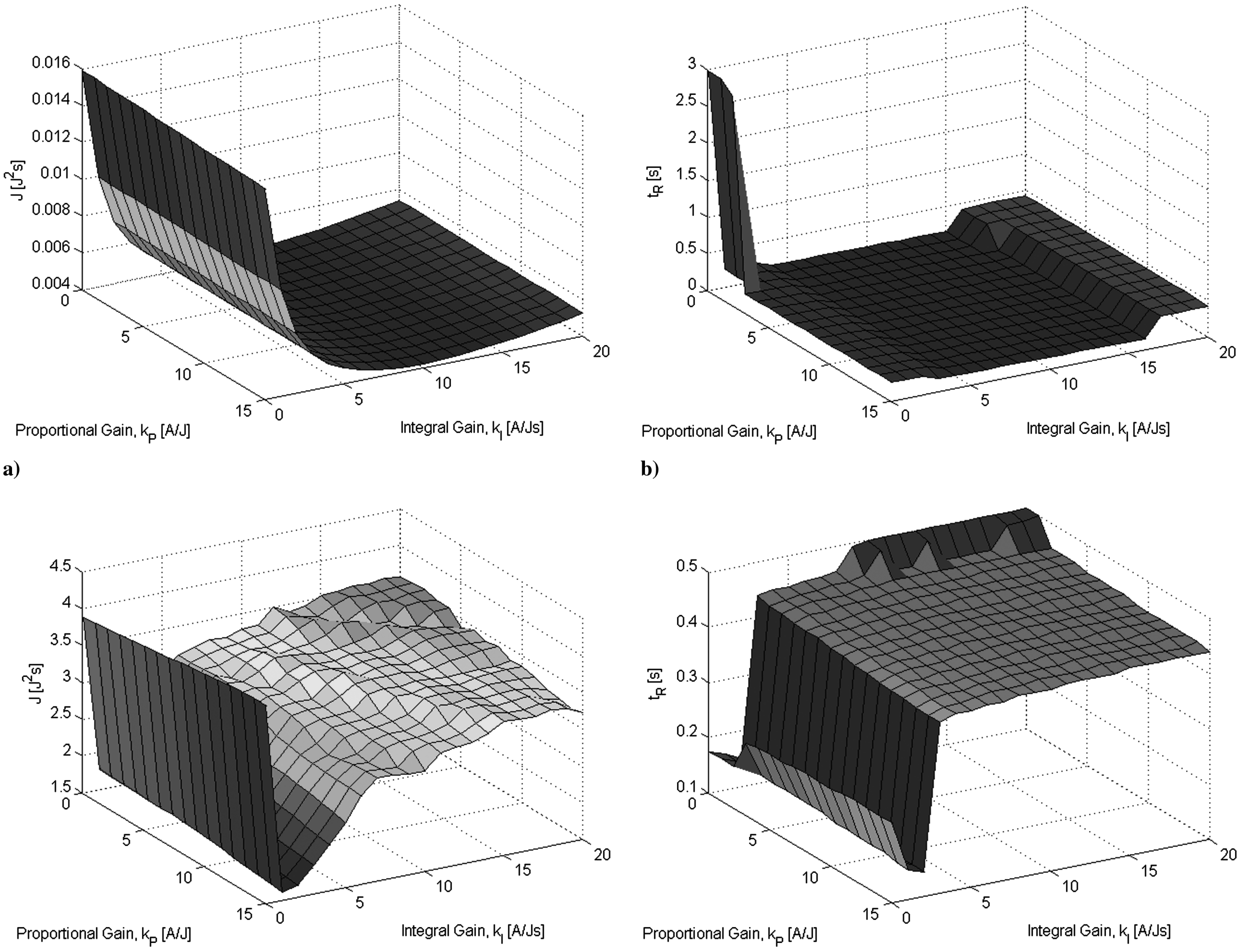

a) b) c) d)

Fig. 12 **Closed-loop gain tuning at 50°: a) error metric at 0.8 mm, b) response time metric at 0.8 mm, c) error metric at 3.4 mm, and d) response time metric at 3.4 mm.**

Recall that there is little variation in the optimal gains in the temperature range of interest. Figure 16 has been included to show how the controller will be modified to account for an amplitude-dependent gain. In this case, the displacement amplitude would be calculated using the same method described in the Open-Loop Design section with a moving average FIR filter.

Simulations were performed to assess the performance of the closed-loop system. Both were able to track the target energy dissipation profile with negligible error, which is an improvement over the open-loop system that had a maximum error near 10%. The difference between these two results was the response time, and this is portrayed in Fig. 17 at an amplitude of 0.8 mm and 30°C. The fixed integral gain value in these simulations is $k_I = 2.8$ A/Js, and the scheduled gain is $k_I(0.8) = 8.3$ A/Js. The proportional gain was set to $k_P = 0$ here. As expected, the figure shows that the scheduled gain controller allows the damper system to settle at the reference dissipation level faster (264 ms) than the fixed gain controller (1.41 s). This provides justification for the consideration of a gain-scheduling controller. Also, note that the oscillations seen in the response are a multiple (twice) of the damper excitation frequency (3.8 Hz) and are artifacts of the averaging that takes place to estimate the energy dissipation and amplitude. The oscillation amplitude shown here is approximately 4% of the target dissipation value.

Experimental Setup

Key components of the experimental setup are shown in Fig. 18. Displacement and force measurements were acquired from a servohydraulic testing machine through its analog readout ports and then fed to the analog-to-digital converters of a PC-based digital control board. One thermocouple was installed inside the MRFE damper, submerged in the fluid, and conditioned by a temperature/process controller to produce a signal that could be recorded using the digital control board. The damper was placed inside an environmental chamber, in which the ambient temperature was controlled using a programmable logic controller employing proportional plus-integral-plus-derivative control with thermocouple feedback. The digital control board then sent a control signal to the digital-to-analog ports and fed a linear power amplifier, which generated the desired current signal to the MRFE damper. The current was monitored in real time by the control system during all tests by recording and displaying a voltage signal output of the amplifier that was proportional to the current output.

While the control simulations were performed at constant displacement amplitudes and temperatures, it is not likely that this is a close approximation to what a typical lag damper would experience during a helicopter mission. Accordingly, a varying displacement amplitude profile was designed to span the range of amplitudes that was provided by the damper manufacturer. Figure 19 shows the amplitude variations. Seven sinusoidal amplitudes were selected to provide an adequate measure of the control system performance at the lag frequency of 3.8 Hz, with the transition between each occurring as a step change. Note that the relative increase or decrease is varied as well. Each amplitude completes 50 cycles before making a step change to the next amplitude level, giving a total of 350 cycles per test (approximately 90 s duration). It should also be noted that the amplitude values and relative changes were selected arbitrarily to span the required amplitude range in a random manner, which is sufficient for an initial demonstration of the capability enabled by the technology. Since the equipment used cannot vary the temperature substantially over this length of time, a number of tests were con-

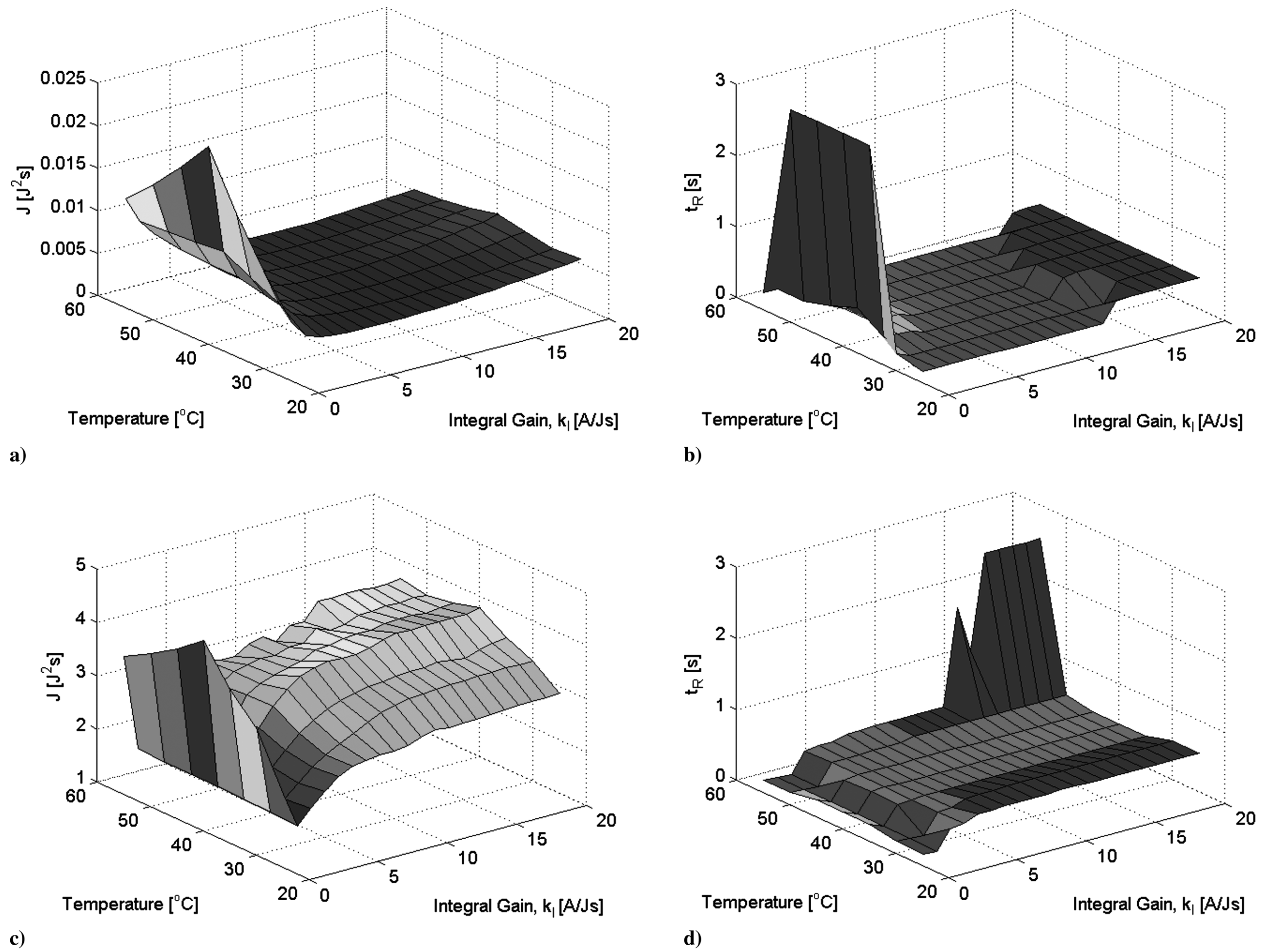

a) b) c) d)

Fig. 13 Integral gain tuning with temperature: a) error metric at 0.8 mm, b) response time metric at 0.8 mm, c) error metric at 3.4 mm, and d) response time metric at 3.4 mm.

ducted in succession while the temperature slowly increased from ambient (∼30°C) to 55°C, using the same amplitude profile for each.

Experimental Control Results

This section presents the results for the three control techniques proposed in this study. The first is the open-loop design where the control current is selected based on real-time measurements of the fluid temperature and displacement amplitude. The second and third techniques are the two closed-loop strategies, both based on PI control (fixed gain and gain scheduling).

Open-Loop Damper Performance

The open-loop control experiments were conducted as described in the previous section. The thermal input was set to rise (slowly), and the damper was exercised several times during this rise to collect data for different temperatures. Note that when the temperature ramp was completed, the thermal input and the control current were turned off, and the tests were performed again as the damper and fluid cooled to establish the field-off performance of the MRFE damper. Comparing the controlled (field-on) results to the baseline (field-off) results helps to highlight the improved performance of the prototype, semi-active damper over the equivalent passive damper. Figure 20 shows

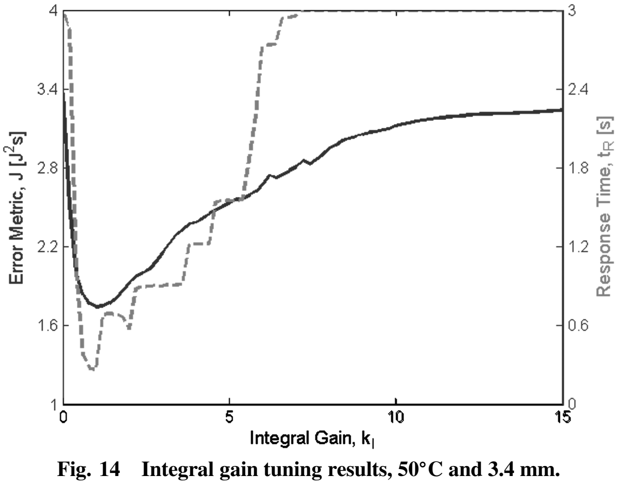

Fig. 14 Integral gain tuning results, 50°C and 3.4 mm.

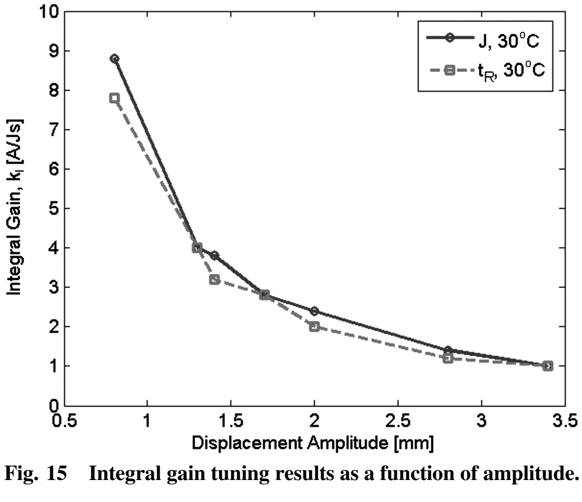

Fig. 15 Integral gain tuning results as a function of amplitude.

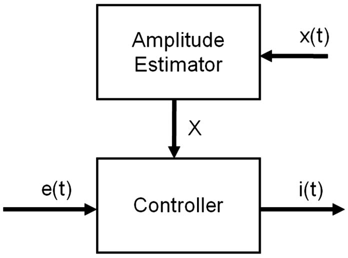

Fig. 16 Gain-scheduling controller approach.

the ability of the open-loop control system to restore performance losses in the passive damper at high temperature. The control current appears in Fig. 20a, with the dark line representing the controller-on case and the light line denoting the controller-off case. For the field-off test, the current simply remains at 0 A for the entire test, but when the controller is active, it follows the designed profile (black dashed line) based on amplitude estimates. There are also spikes in the current signals here, but this is due to the testing machine, which must momentarily stop before switching excitation amplitudes. However, the controller computations continue to take place with the result shown. Figure 20b shows the corresponding energy dissipation at each of the displacement amplitudes for the controlled case (dark) and uncontrolled case (light). The clear distinction between energy dissipation levels at 53°C, ranging from as much as a 200% increase at the smallest amplitude (0.8 mm) to as low as an 80% increase at the largest amplitude (3.4 mm), highlight the controllable range of the prototype MRFE lag damper.

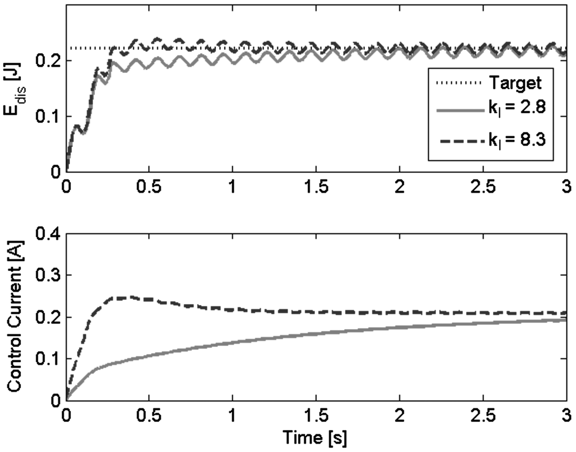

Fig. 17 Performance comparison of closed-loop approaches, 0.8 mm and 30°C.

Figure 21 shows how the open-loop controller performs over the tested temperature range. The target energy dissipation profile appears as the black dashed line and, for this demonstration, it is a function of only displacement amplitude. Thus, the shown energy dissipation profile is desired to remain constant over the temperature range tested. The circles denote 30°C, which was the lowest temperature tested here, the squares denote 41°C, and the diamonds denote 53°C, which was the highest temperature tested here. In the field-off (no control) condition (light), there is a clear trend in the damper of decreasing energy dissipation as the temperature increases, and this has been noted previously in temperature characterization data [10,11]. Incidentally, this characteristic also served as motivation for exploring the prototype device with damping restoration capabilities. The controlled results (dark) show that this ability was achieved with the MRFE damper using open-loop control. While there is some variation about the target profile, it should be noted that this variation does not follow the consistent trend evident in the field-off data. That is, with the open-loop controller active, the two extremes of the temperature range cause slight negative errors (E_{dis} higher than target), although a temperature in the middle causes a slight positive error (E_{dis} lower than target). Some variation should be expected, given that this is an open-loop controller that must interpolate between discrete amplitudes (six values) and temperatures (four values) based on measured signals. However, it should be noted that the maximum error for the controlled results over the entire amplitude range and temperature range is only −11.8%, occurring at 53°C with an amplitude of 0.8 mm. Note that the field-off energy dissipation at this test condition is below the desired point by 62.6%. Also worth noting is the overall average deviation from the target profile for the open-loop controlled case, which is only 3.3%.

The most straightforward approach to increase the accuracy of the open-loop controller would be to parameterize the lookup table entries over a finer resolution of displacement amplitudes and temperatures. However, this would require characterization experiments to be performed at each new test condition. Given that the present controller has a maximum single-point error of 11.8% and an

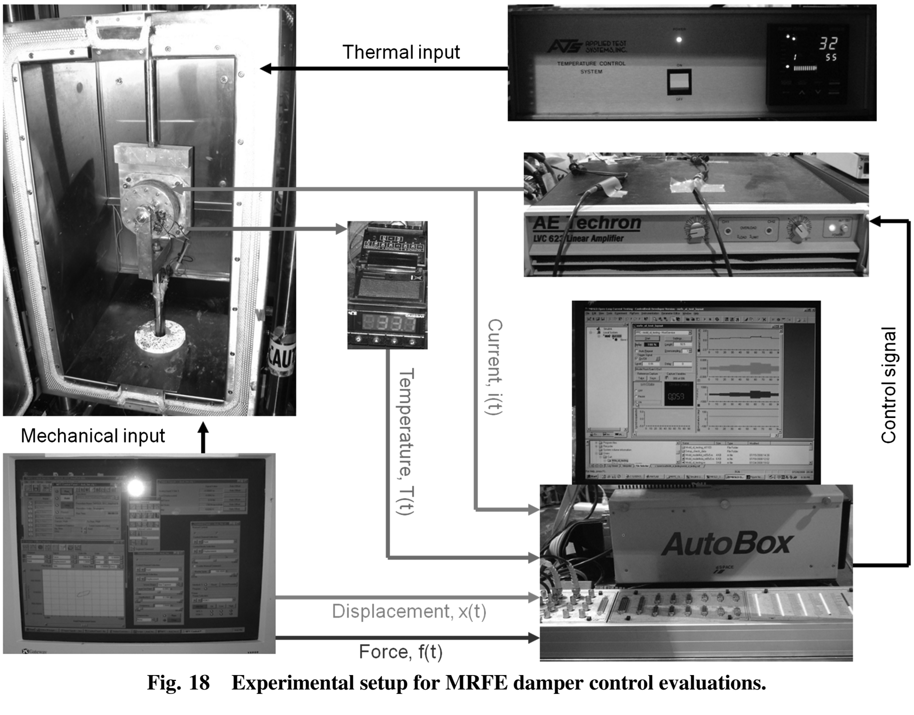

Fig. 18 Experimental setup for MRFE damper control evaluations.

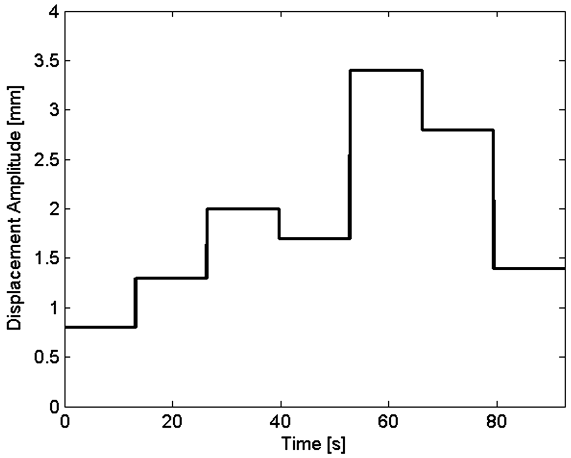

Fig. 19 Designed displacement amplitude variation.

overall error average of only 3.3%, this evaluation has validated the controller form. Additionally, this experimental confirmation of the controller also provides more validation for the hydromechanical model and its utility in designing a control system.

Closed-Loop Damper Performance

Before beginning the closed-loop control evaluations, a number of individual tests were run to verify that the gains chosen from the simulations corresponded well with the experiment. While the simulation study could easily vary a number of parameters in a short time, performing the same optimization manually in the experiment would require a substantial amount of time and effort, so only the ambient temperature (30°C) was used here, and only three amplitudes were considered (0.8, 1.4, and 3.4 mm). Sample results collected at a 3.4 mm displacement amplitude are shown in Fig. 22 for varying the integral gain with $k_P = 0$. Here, the solid line corresponds to the cumulative error J, and the dashed line shows the response time metric t_R. Considering, first, the value of J, it can be seen that the minimum occurs when $k_I = 3$, which is higher than that predicted ($k_I = 1.0$), but it is on the same order of magnitude. However, the gain at which the response time metric t_R is minimum ($k_I = 1.5$) is closer to the predicted value ($k_I = 1.0$). Recall that the optimal value of the two performance metrics coincided during the design simulations, which is not the case here. Since J does not vary substantially between $k_I = 1.5$ and $k_I = 3$, the decision was made to use the minimum response time gain, $k_I = 1.5$, as the ideal gain at this test condition. It should also be mentioned that the magnitude of the performance metrics vary somewhat from the design case. This is likely attributable to measurement noise present in the experiment and minor discrepancies between the mathematical model and the prototype MRFE lag damper.

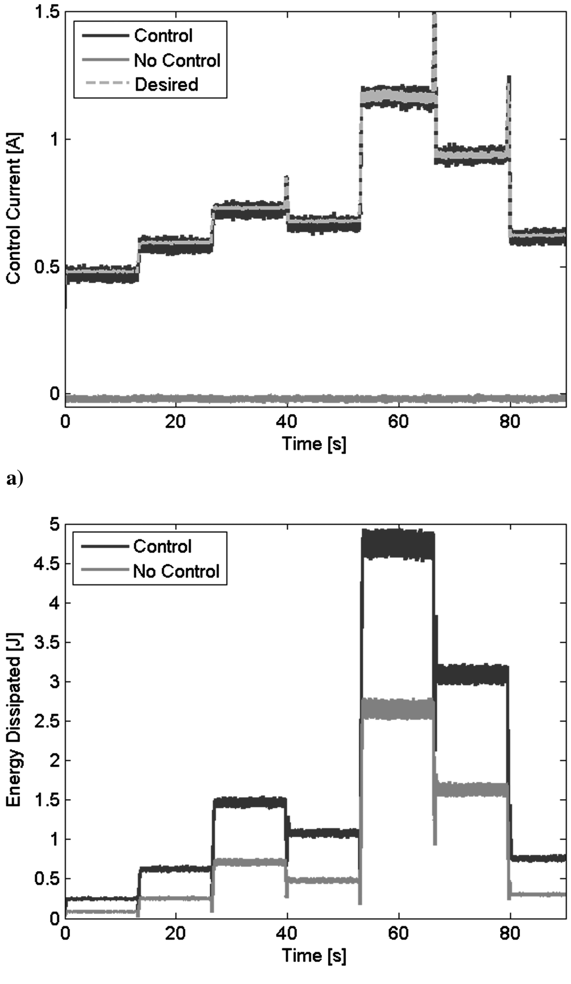

a)

b)

Fig. 20 Experimental results from open-loop control test at 53°C: a) control current and b) energy dissipation.

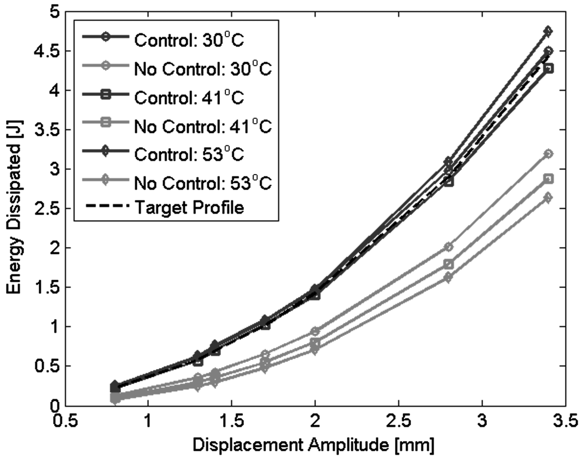

Fig. 21 Experimental results from open-loop MRFE control test.

While the simulations showed little effect on the response from varying the proportional gain k_P, this term was added to the experimental controller to potentially increase performance. Accordingly, the integral gain was fixed at the preferred value of $k_I = 1.5$ A/Js, and a number of tests were run with varying k_P values. These results are shown in Fig. 23 for a displacement amplitude of 3.4 mm and temperature of 30°C. At 3.4 mm, the simulations showed that a low proportional gain would be slightly preferred according to the response time metric (Fig. 12d), although a high proportional gain

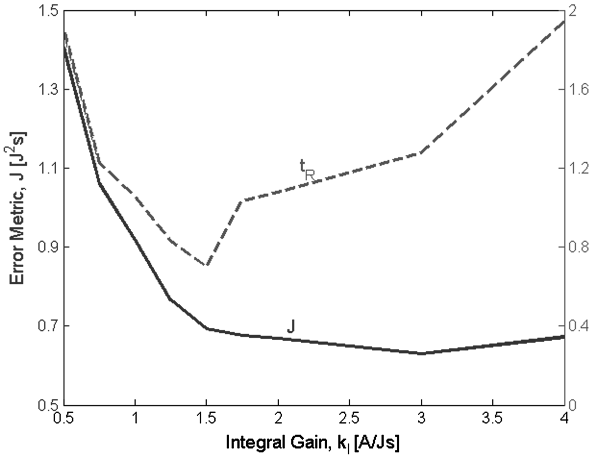

Fig. 22 Experimental integral gain tuning, 3.4 mm and 30°C.

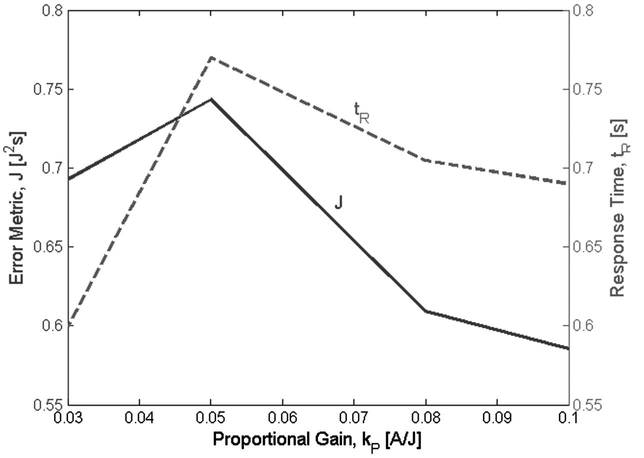

Fig. 23 Experimental proportional gain tuning, 3.4 mm and 30°C.

would be slightly preferred according to the error metric (Fig. 12c). Being that the performance improvement from k_P at either metric is relatively low, priority was given to the response time, which called for a low proportional gain. Hence, the region of manually checking proportional gains in the experimental control system limited k_P to the low values shown. A minimum of the two metrics does not coincide and does not even appear in the tested range. While this tends to indicate that exploring higher or lower gain values may produce a minimum in the plot, the preferred proportional gain at this condition was set to $k_P = 0.03$ A/J, because the lowest tested response time occurred here and because response time was given priority. Lower values could have been tested as well, but they begin to approach $k_P = 0$, which was shown in Fig. 22 to cause a slower response. With $k_P = 0$ (Fig. 22), the fastest time achieved was 0.8 s, but when $k_P = 0.03$, this response time metric dropped to 0.6 s. This shows that nearly a 25% reduction was possible by adding this low-valued proportional gain to the closed-loop system. Hence, by combining the results of Fig. 22 with Fig. 23, a minimum in response time with respect to k_P does exist at the selected value. Higher k_P values were not tested for a number of reasons. First, the figure shows a trend of diminishing returns in regard to the two performance metrics. Second, the closed-loop simulations showed minimal effect from varying k_P. Third, higher gains would call for a larger control current, which would require more power for the system for little gain in performance, thereby reducing overall efficiency of the device.

Similar experiments were also conducted at the other two amplitudes mentioned, using both integral and proportional gains, and the final selected gain values are displayed in Fig. 24. The same trends are seen in both gain values. That is, larger amplitudes require smaller control gains. This is also the general trend that was predicted in the closed-loop control simulations, but it appears to be more linear here in both gains and more pronounced for the proportional gain. It needs to be noted that the ideal gain values do change a relatively large amount over the amplitude range of interest (approximately one order of magnitude). Since the gain values do appear to vary linearly with amplitude, the average values (marked in the figure) were the designated closed-loop control gains for the first experimental evaluation. A loss in performance is certainly expected (being more pronounced at the extremes), but this is one of the tradeoffs that must be made to maintain a simpler control strategy. The fixed gain control parameters are hence $k_P = 0.31$ A/J and $k_I = 4.75$ A/Js. For the gain-scheduling version, the values in Fig. 24 were used in interpolation tables and were selected with the FIR filter that estimates displacement amplitude.

An example data set from the experimental closed-loop evaluations is shown in Fig. 25 for 51°C. This data is for the gain-scheduling controller, although the fixed gain controller performed quite similarly. The energy dissipation tracking appears in the upper plot, with the solid line indicating the controlled response and the dashed line representing the desired response. The controlled response overlays the reference signal for the majority of the time at each amplitude level, with the exception of the transient periods after the step changes in displacement amplitude occur. This tends to create an impulsive behavior in the calculations, including the reference energy dissipation profile, which is computed based on the estimated amplitude measurement. Although the amplitude changes are preprogrammed into the test machine, recall that there is a momentary stop between changes that causes a spike in the estimates. This effect was also seen in the open-loop testing. The lower plot shows the corresponding control current, which repeats the impulsive behavior. The closed-loop design indicated that less than

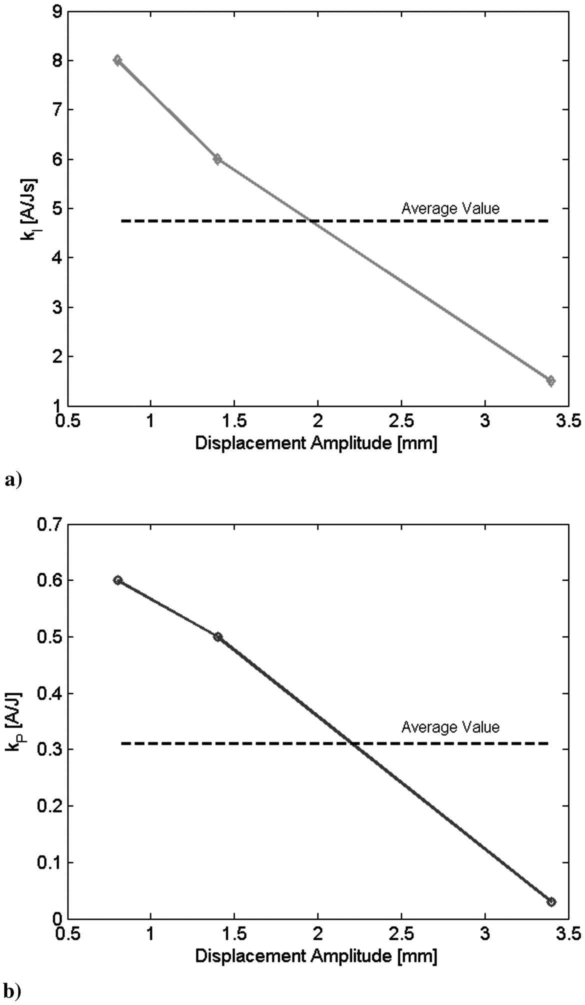

Fig. 24 Experimental closed-loop gain tuning at 30°C: a) integral gain and b) proportional gain.

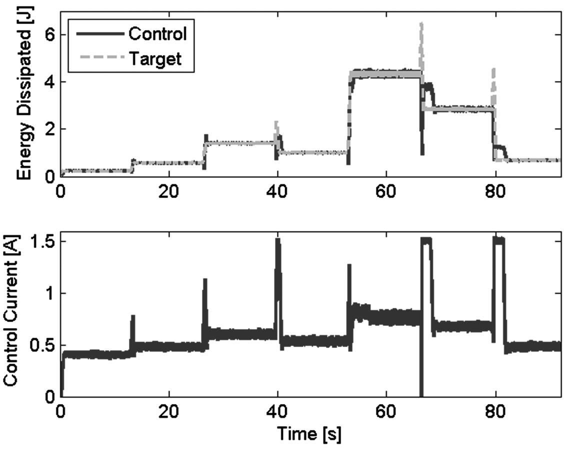

Fig. 25 Experimental closed-loop gain-scheduling results at 51°C.

1 A would be needed for proper tracking, so it should be noted here that the current was limited to 1.5 A during these experiments to provide some margin. However, the impulsive nature of the test system led to brief durations of current saturation when the amplitude decreased. Aside from this machine-related issue, the closed-loop systems performed well.

To show how accurate the closed-loop tracking capability was across the tested temperature range, averages were computed from the energy dissipation data from each of the nine temperature tests and compared with the reference dissipation profile. The starting point for the averages was taken to be just after the transients died out, and the ending point was just before the next step change. Thus, the averages reflect the steady-state values. This was done at each of the nine temperatures, and then the results at each of the different amplitude levels were averaged over the temperature range to give an overall average. Figure 26a highlights the performance of the closed-loop systems. The controlled energy dissipation with fixed gains (circles) and scheduled gains (diamonds) falls directly on the target profile for the entire amplitude range tested. Since these data points do represent average values, it should be noted that the largest steady-state error calculated at any amplitude or temperature condition was less than 0.2%. However, minimal steady-state error is to be expected with the control technique used here. That is, the PI controller continuously adjusts the control signal until the error (input to controller) becomes zero. The time it takes to reach steady state then becomes a useful performance comparison between the two closed-loop approaches tested, and it was the motivation to explore the scheduled gain approach (recall Fig. 17).

Figure 26b provides a picture of how the two closed-loop techniques compare in terms of response time across the amplitude range tested. Each data point shown represents the average response time across all temperatures at its corresponding amplitude, where it can be seen that all are around 1 s. There are two amplitudes where the scheduled gains actually cause a slower system response (1.4 and 2.8 mm). This was unexpected, but when looking back at the time history data, it is these two amplitudes that correspond to the largest two amplitude decreases. As it turns out, the servohydraulic test machine used in the experiments was unable to smoothly transition from one amplitude to the next without first momentarily stopping. The combination of this pause and the continual calculations of the control system led to impulsive estimates of the amplitude and damping, which caused control current saturation in these instances. This effect was largest in both the open-loop and closed-loop experiments at these two amplitudes as well. The gain-scheduling technique was employed after completing the fixed gain experiments in an attempt to increase the speed of response in bringing the energy dissipation of the prototype MRFE damper to a desired level. While this was successful at five of the seven amplitudes tested, the improvement in speed (decrease in settling time) was relatively small. By this result, it may be concluded that the added complexity of the gain-scheduling controller is not worth the nominal improvement in performance, but this decision should ultimately be made by the system integrator.

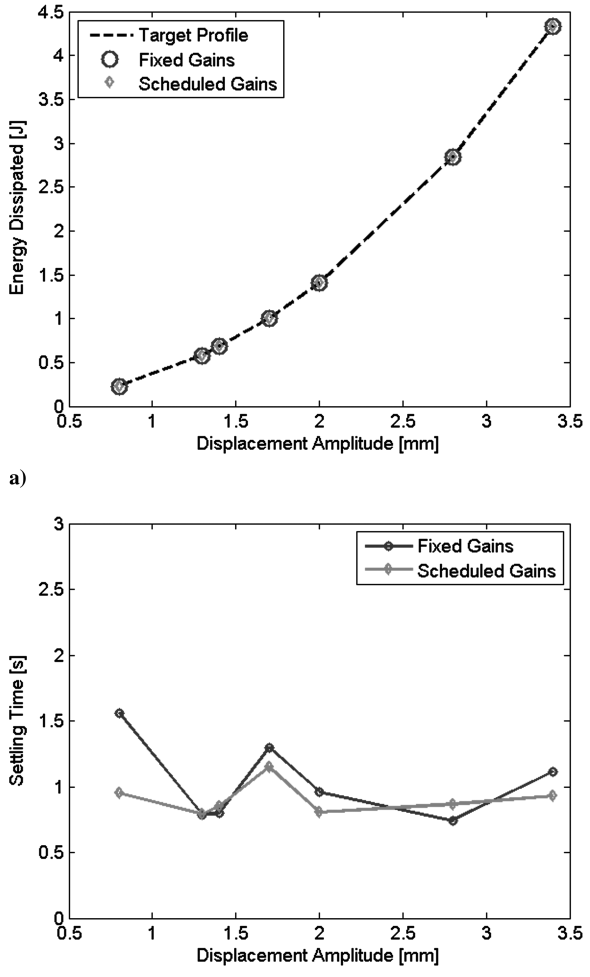

a)

b)

Fig. 26 Experimental results from closed-loop MRFE control tests: a) energy dissipation and b) settling time.

Conclusions

A semiactive FE lag damper with field-controllable MR fluid was evaluated in the fixed frame for its ability to track a reference damping profile and restore performance losses due to increasing temperatures and variations in displacement amplitude. The primary conclusion of this work is that relatively simple open-loop and closed-loop control techniques are sufficient for enabling a modified snubber-type damper to dissipate a desired, or prescribed, amount of energy as it experiences changes in input displacement and ambient temperature that may otherwise affect its baseline uncontrolled performance. Measured results indicated that both the open-loop (lookup table) and closed-loop (fixed PI and gain-scheduled PI) control schemes had the ability to compensate for changes in displacement amplitude and temperature. In comparing the performances of the control approaches, it was concluded that the two closed-loop formulations more accurately tracked the desired performance level than the open-loop approach, although the preferred technique of the two closed-loop approaches was less clear. A secondary conclusion based on the successful experimental results is that the form of the hydromechanical model for the damper behavior is an acceptable analytical tool for use in designing and investigating the performance of various control techniques. Having demonstrated the performance of the MRFE lag damper in the fixed frame, the next step in its development is evaluation in the rotating frame.

Acknowledgments

This work was supported by the Defense Advanced Research Projects Agency (DARPA) Phase II Small Business Innovation Research, contract number W31P4Q06C0400, with technical monitor Daniel Newman. The second author (G. Ngatu) thanks the Alfred P. Sloan Foundation for fellowship support. The views and conclusions contained in this document are those of the authors and should not be interpreted as representing the official policies, either express or implied, of the DARPA or the U.S. Government. The laboratory prototype was a modified Bell 430 lag damper (Fluidlastic® FL-1030-8), and the authors thank Lord Corporation for providing these dampers to the project, as well as technical discussions on damper and magnetorheological fluid design and usage.

References

[1] Panda, B., Mychalowycz, E., Kothman, B., and Blackwell, R., "Active Controller For Comanche Air Resonance Stability Augmentation," *Proceedings of the 55th American Helicopter Society Annual Forum*, Baltimore, MD, AHS International, Alexandria, VA, June 1999.

[2] Zhao, Y., Choi, Y. T., and Wereley, N. M., "Semi-Active Damping of Ground Resonance in Helicopters Using Magnetorheological Dampers," *Journal of the American Helicopter Society*, Vol. 49, No. 4, 2004, pp. 468–482.
doi:10.4050/JAHS.49.468

[3] Jones, P., Russell, D., and McGuire, P., "Latest Development in Fluidlastic® Lead–Lag Dampers for Vibration Control in Helicopter," *Proceedings of the 59th American Helicopter Society Annual Forum*, Phoenix, AZ, AHS International, Alexandria, VA, May 2003.

[4] Snyder, R., Krishnan, R., Wereley, N., and Sieg, T., "Mechanisms Based Analysis of Elastomeric Lag Damper Behavior Under Single and Dual Frequency Excitation Including Temperature Effects," *Proceedings of the 57th American Helicopter Society Annual Forum*, Washington, DC, AHS International, Alexandria, VA, May 2001.

[5] Panda, B., Mychalowycz, E., and Tarzanin, F., "Application of Passive Dampers to Modern Helicopters," *Smart Materials and Structures*, Vol. 5, No. 5, 1996, pp. 509–516.
doi:10.1088/0964-1726/5/5/001

[6] Hu, W., and Wereley, N. M., "Distributed Rate-Dependent Elastoslide Model for Elastomeric Lag Dampers," *Journal of Aircraft*, Vol. 44, No. 6, 2007, pp. 1972–1984.
doi:10.2514/1.26409

[7] Felker, F., Lau, B., McLaughlin, S., and Johnson, W., "Nonlinear Behavior of an Elastomeric Lag Damper Undergoing Dual-Frequency Motion and its Effect on Rotor Dynamics," *Journal of the American Helicopter Society*, Vol. 32, No. 4, 1987, pp. 45–53.
doi:10.4050/JAHS.32.45

[8] Wereley, N. M., Snyder, R., Krishnan, R., and Sieg, T., "Helicopter Damping," *Encyclopedia of Vibration*, Vol. 2, Academic Press, London, 2001, pp. 629–642.

[9] McGuire, D. P., "Fluidlastic Dampers and Isolators for Vibration Control in Helicopters," *Proceedings of the 50th American Helicopter Society Annual Forum*, Washington, D.C., AHS International, Alexandria, VA, May 1994.

[10] Marr, C., Lesieutre, G. A., and Smith, E. C., "Nonlinear, Temperature-Dependent, Fluidlastic Lead–Lag Damper Modeling," *Proceedings of the 64th American Helicopter Society Annual Forum*, Montreal, AHS International, Alexandria, VA, April 2008.

[11] Ngatu, G. T., Kothera, C. S., and Wereley, N. M., "Hydro-Mechanical Modeling of a Fluidlastic Lag Damper Incorporating Temperature Effects," *Proceedings of the 65th American Helicopter Society Annual Forum*, Grapevine, TX, AHS International, Alexandria, VA, May 2009.

[12] Kamath, G. M., Wereley, N. M., and Jolly, M. R., "Characterization of Magnetorheological Helicopter Lag Dampers," *Journal of the American Helicopter Society*, Vol. 44, No. 3, 1999, pp. 234–248.
doi:10.4050/JAHS.44.234

[13] Hu, W., and Wereley, N. M., "Magnetorheological Fluid and Elastomeric Lag Damper for Helicopter Stability Augmentation," *International Journal of Modern Physics. B, Condensed Matter Physics, Statistical Physics, Applied Physics*, Vol. 19, Nos. 7–9, 2005, pp. 1527–1533.
doi:10.1142/S0217979205030542

[14] Hu, W., Wereley, N. M., Chemouni, L., and Chen, P. C., "Semi-Active Linear Stroke Magnetorheological Fluid–Elastic Helicopter Lag Damper," *Journal of Guidance, Control, and Dynamics*, Vol. 30, No. 2, 2007, pp. 565–575.
doi:10.2514/1.24033

[15] Hu, W., and Wereley, N. M., "Hybrid Magnetorheological Fluid Elastomeric Dampers for Helicopter Stability Augmentation," *Smart Materials and Structures*, Vol. 17, No. 4, 2008, Paper 045021.
doi:10.1088/0964-1726/17/4/045021

[16] Marathe, S., Gandhi, F., and Wang, K. W., "Helicopter Blade Response and Aeromechanical Stability with a Magnetorheological Fluid Based Lag Damper," *Journal of Intelligent Material Systems and Structures*, Vol. 9, No. 4, 1998, pp. 272–282.
doi:10.1177/1045389X9800900405

[17] Gandhi, F., Wang, K. W., and Xia, L., "Magnetorheological Fluid Damper Feedback Linearization Control for Helicopter Rotor Application," *Smart Materials and Structures*, Vol. 10, No. 1, 2001, pp. 96–103.
doi:10.1088/0964-1726/10/1/309

[18] "Magnetic Circuit Design," Engineering Note, Lord Corp., Cary, NC, 1999, http://www.docstoc.com/docs/24848545/Magnetic-Circuit-Design [retrieved 5 May 2011].

[19] Ngatu, G. T., Hu, W., Kothera, C. S., and Wereley, N. M., "Effects of Temperature on Magnetorheological Snubber Lag Damper for Bearingless Helicopter Main Rotor," 50th AIAA Structures, Structural Dynamics, and Materials Conference, Palm Springs, CA, AIAA Paper 2009-2110, May 2009.

[20] Ngatu, G. T., Hu, W., Wereley, N. M., and Kothera, C. S., "Adaptive Snubber-Type Magnetorheological fluid-elastomeric Helicopter Lag Damper," *AIAA Journal*, Vol. 48, No. 3, 2010, pp. 598–610.
doi:10.2514/1.43356

[21] Mitra, S. K., *Digital Signal Processing: A Computer-Based Approach*, 2nd ed., McGraw–Hill, New York, 2001, pp. 86–89.